

Contrast Enhancement by Feedback Fields in Magnetic Resonance Imaging[†]

Sandip Datta, Susie Y. Huang, and Yung-Ya Lin*

Department of Chemistry and Biochemistry, University of California, Los Angeles, California 90095

Received: January 31, 2006; In Final Form: April 25, 2006

A conceptually new approach giving rise to contrast enhancement by feedback fields in magnetic resonance imaging is proposed, and the detailed mechanism is described. Nonlinear spin dynamics under the feedback fields of the distant dipolar field and/or radiation damping are examined and shown to amplify contrast due to small variations in spin density and precession frequency. Feedback-based contrast enhancement depends on the instability of the initial magnetization configuration and is propagated by positive feedback, as shown through numerical simulations and experimental results on simple phantom samples. On the basis of a theoretical understanding of contrast enhancement, insight into pulse sequence design and optimal contrast attainable under the individual and joint feedback fields is provided.

I. Introduction

Magnetic resonance imaging (MRI) and its high spatial resolution cousin, MR microscopy, are endowed with an abundance of contrast-generating MR parameters sensitive to a wide range of tissue and material properties.^{1,2} Despite the diversity of MR contrast origins, contrast can still be a limiting factor if the MR properties of interest do not vary appreciably, thereby obscuring the underlying morphology. Such lack of contrast is especially problematic in biomedical MRI, where contrast is crucial to identifying the presence and extent of pathology. Targeting this problem, a new approach is demonstrated here to enhance MRI contrast due to small variations in MR properties by exploiting emergent, nonlinear feedback interactions. Such avalanching amplification of MRI contrast relies on intricate mechanisms unified by the concepts of dynamical instability and positive feedback, as manifested in the resulting spin dynamics.

In this paper, we propose and demonstrate mechanisms leading to contrast enhancement under two feedback or reaction fields, the distant dipolar field³ (DDF) and radiation damping.⁴ Factors leading to better sensitivity in MRI, e.g., higher fields, more sensitive probes, and larger equilibrium polarization, also promote the development of these nonlinear feedback interactions. The DDF and radiation damping depend explicitly on the distribution of spins or magnetization in the sample and render the dynamics nonlinear. The nonlinear dynamical process acts as a feedback loop: the magnetization distribution generates the field, and the resulting field in turn determines the subsequent magnetization distribution. In particular, radiation damping is a feedback field mediated by the coupling between the bulk magnetization and the receiver coil, whereas the DDF is primarily determined by the local distribution of magnetization surrounding the position or voxel at which the field is calculated. For certain magnetization configurations, the dynamics under the individual or joint reaction fields may become unstable. Due to such dynamical instability, nonlinear feedback processes can be initiated in the presence of these fields to amplify small

variations in the magnetization distribution, which in turn reflect the spatial distribution of MR properties, such as spin density or precession frequency. Growing variations in the magnetization distribution under the feedback fields subsequently change the resulting magnetization-dependent fields, which act to reinforce differences in the magnetization distribution. As the contrast due to small variations in MR parameters builds up through this mechanism, the overall dynamical process giving rise to contrast enhancement exhibits positive feedback. In particular, avalanching amplification of MRI contrast occurs when the perturbations to an unstable magnetization configuration are spatially coherent and represent distinct structures in the sample.

This work focuses on elucidating the mechanisms responsible for contrast enhancement under the individual and joint feedback fields. We first establish the dynamical equation of motion and model system that will be used to understand the complex spin dynamics. Sections III, IV, and V explain in detail the specific contrast enhancement mechanisms under the DDF, radiation damping, and the joint feedback fields, respectively. Experimental results on simple phantoms are provided to support the described mechanisms. Finally, we discuss the relative advantages of each mechanism in imaging experiments and suggest ways to optimize the attainable contrast enhancement under the feedback fields.

II. Nonlinear Bloch Equations

In MRI, the time evolution of the magnetization in a voxel at position \mathbf{r} , $\mathbf{m}(\mathbf{r}, t) \equiv \mathbf{M}(\mathbf{r}, t)/M_0$ (normalized with respect to the equilibrium magnetization of pure water M_0), in the rotating frame of angular frequency ω_0 can be approximated by the classical Bloch equations:⁵

$$\frac{\partial \mathbf{m}(\mathbf{r}, t)}{\partial t} = \gamma \mathbf{m}(\mathbf{r}, t) \times \left[\frac{\delta \omega(\mathbf{r})}{\gamma} \hat{\mathbf{z}} + \mathbf{B}(\mathbf{r}, t) \right] - \frac{m_z(\mathbf{r}, t) - m_{eq}(\mathbf{r})}{T_1(\mathbf{r})} \hat{\mathbf{z}} - \frac{m_x(\mathbf{r}, t)\hat{\mathbf{x}} + m_y(\mathbf{r}, t)\hat{\mathbf{y}}}{T_2(\mathbf{r})} + D(\mathbf{r})\nabla^2 \mathbf{m}(\mathbf{r}, t) \quad (1)$$

where $m_{eq}(\mathbf{r}) \equiv M_{eq}(\mathbf{r})/M_0$ is the normalized equilibrium magnetization at position \mathbf{r} , γ is the gyromagnetic ratio, $\delta \omega \equiv \omega - \omega_0$ is the resonance offset of the magnetization from the

* To whom correspondence should be addressed. E-mail: yylin@chem.ucla.edu.

[†] Part of the special issue "Charles M. Knobler Festschrift".

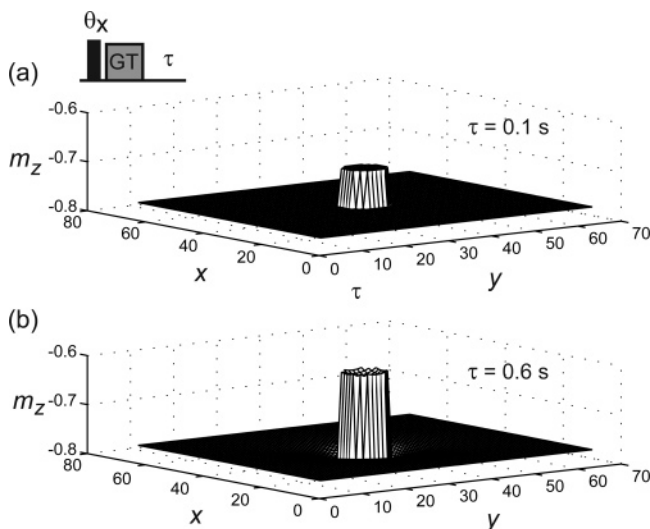


Figure 1. Evolution of m_z in a transverse plane along the z -axis under the DDF only, following the pulse sequence shown ($\theta = 110^\circ$), for a model system with a small difference in spin density $\delta m = 0.1$ between the inner (I) and outer (O) regions. (a) $\tau = 0.1$ s; (b) $\tau = 0.6$ s. Spin density in region O is 1, whereas spin density in region I is 0.9. The x - and y -directions are labeled by the index of spatial grid points. Dynamics were simulated by numerically integrating the nonlinear Bloch equations without relaxation or diffusion terms ($(GT)_z = 5$ G·ms/cm, $\tau_d = 69$ ms).

rotating frame frequency ω_0 , $\mathbf{B}(\mathbf{r}, t)$ is the local field, T_1 and T_2 are the longitudinal and transverse relaxation times, respectively, and D is the diffusion coefficient. The voxels are assumed to be small volumes with uniform spin density, such that a single voxel does not contain more than one type of tissue. To simplify our discussion of the contrast enhancement mechanisms, the relaxation and diffusion terms will not be considered here.

In the following three sections, contrast enhancement under various nonlinear feedback interactions is examined using a model system consisting of two regions differing in a specific MR parameter, *i.e.*, proton density or precession frequency. All numerical results reported in this paper were obtained using MATLAB (The Mathworks, Inc., South Natick, MA) on personal computers. The sample was modeled by a cube of sides 0.4697 mm each sampled by $64 \times 64 \times 32$ voxels in the x -, y -, and z -directions. A cylinder of radius 0.0367 mm (sampled by 5 voxels across) was placed at the center of the cube (Figure 1). Equation 1 (without relaxation and diffusion) was numerically integrated by the finite-difference method and Runge–Kutta(4,5) formula with a relative error tolerance of 0.001. The simulations were carried out for a resonance frequency of 600 MHz and the value of equilibrium magnetization was 0.0426 A/m. The gradient strength employed for the simulation was $(GT)_z = 5$ G·ms/cm. The values of radiation damping and the DDF time constants were $\tau_r = 8$ ms and $\tau_d = 69$ ms, respectively. The DDF was calculated using the numerical procedure outlined in ref 6. We assume that the spins inside the cylinder, designated as region I, possess slightly different MR parameter(s) than the spins on the outside, designated as region O. Contrast is defined by $\Delta\langle m_z \rangle_z \equiv \langle m_z(\mathbf{r}_O, t) \rangle_z - \langle m_z(\mathbf{r}_I, t) \rangle_z$, where $\langle m_z(\mathbf{r}, t) \rangle_z$ denotes the average of m_z along the z -direction for a voxel at position \mathbf{r} .

III. Distant Dipolar Field

Dipolar couplings between distant spins are not averaged out by diffusion in liquids and in general give rise to an interaction

that is not local.⁷ The secular part of the DDF $\mathbf{B}_d(\mathbf{r}, t)$ is given by³

$$\gamma \mathbf{B}_d(\mathbf{r}, t) = \frac{1}{4\pi\tau_d} \int d\mathbf{r}' \frac{3\cos^2\theta_{rr'} - 1}{2|\mathbf{r} - \mathbf{r}'|^3} \times [3m_z(\mathbf{r}', t)\hat{\mathbf{z}} - m(\mathbf{r}', t)], \quad (2)$$

where the DDF time constant $\tau_d = 1/\gamma\mu_0 M_0$ in S. I. units and $\theta_{rr'}$ is the angle between the internuclear vector and the external magnetic field $B_0\hat{\mathbf{z}}$. For the specific case in which the magnetization is modulated along a single direction, *e.g.*, z , the DDF may be approximated as a local function of the magnetization:^{3,8,9}

$$\gamma \mathbf{B}_d(z, t) = \frac{1}{4\pi\tau_d} \left\{ \frac{1}{3} [\mathbf{m}(z, t) - \langle \mathbf{m} \rangle] - [m_z(z, t) - \langle m_z \rangle] \hat{\mathbf{z}} \right\} \quad (3)$$

The dependence of the DDF on the magnetization distribution causes it to act as a feedback field as follows. Under the dipolar interaction, a given spin polarizes the surrounding spins; changes in the neighboring spin states later act back through the DDF to affect the tagged spin's subsequent evolution. Certain configurations of magnetization have been shown to be linearly unstable under the DDF.^{10,11} For example, consider the magnetization grating or helix created by a pulse-gradient combination $[\theta - GT]$ on a sample of uniform spin density, the evolution of which can be described by combining eqs 1 and 3.

Under the DDF only, a perfect helical distribution of magnetization is stationary, *i.e.*, does not evolve, to zeroth order, as is shown in the perturbation treatment in ref 11. However, small initial deviations from a perfect helical distribution grow exponentially in time, eventually generating an increasingly large number of spatial frequency components at long times. For a sample with slight nonuniformities in the underlying MR properties, *e.g.*, spin density, the initial magnetization configuration created by $[\theta_x - (GT)_z]$ is already not stationary to zeroth order under the DDF. However, if the difference in spin density δm is small, the magnetization configuration evolves away from its initial state under the DDF in a manner that approximately mimics the dynamics of a perturbed, linearly unstable magnetization helix with uniform spin density. This evolution generates successive nonuniform magnetization configurations in time that increasingly reflect the distribution of MR properties through positive feedback (Figure 1).

Intermolecular multiple quantum coherences (iMQCs) generated under the DDF have been used to provide distance-selected contrast sensitive to differences in resonance frequency and magnetization density.¹² When the initial variation in MR properties is spatially coherent and mirrors actual structural variations in the sample, the instability induced by the DDF can also be used to enhance contrast due to such MR properties. For example, following $[\theta_x - (GT)_z]$, the magnetization distribution is the sum of modulation in two directions: a fully modulated, periodic variation along the z -axis and a small amplitude, step function-like modulation in the transverse plane. Assume that the magnetization inside the cylinder in region I has a slightly smaller proton density differing by δm than the magnetization on the outside in region O. To gain insight into how a magnetization helix with nonuniform spin density evolves under the DDF, it is instructive to consider first the dynamics of a perfect magnetization helix with uniform spin density modulated in a single direction as a point of comparison. In this case, the one-dimensional approximation of the DDF (eq 3) indicates that the transverse magnetization, $m_+(\mathbf{r}, t) \equiv$

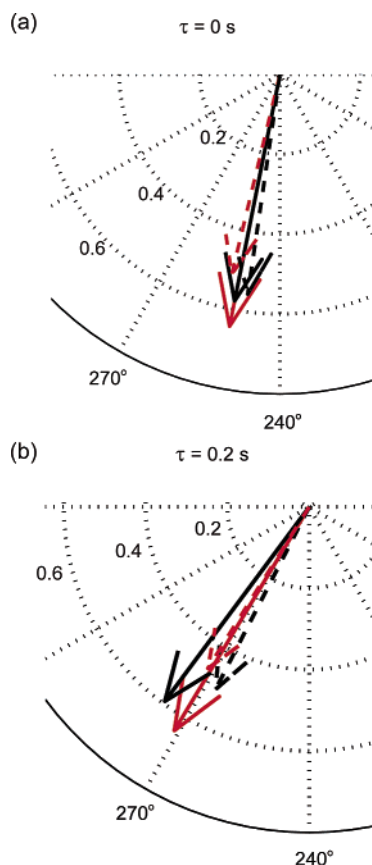


Figure 2. The transverse components of the magnetization, $m_+(r,t)$ (solid line), and the corresponding DDF, $B_{d,+}(r,t)$ (dashed line), for a voxel in region O (black, $(x_0, y_0, z_0) = (8, 16, 8)$) and region I (red, $(x_1, y_1, z_1) = (28, 28, 8)$) in the same xy -plane, plotted as vectors (a) immediately after the application of the pulse sequence in Figure 1 and (b) at $\tau = 0.2$ s. Simulation parameters are the same as in Figure 1.

$m_x(r,t) + im_y(r,t)$, and the corresponding transverse components of the DDF, $B_{d,+}(r,t) \equiv B_{d,x}(r,t) + iB_{d,y}(r,t)$, are aligned at all times. The contributions to $B_{d,+}(r,t)$ in a given xy -plane from $m_+(r,t)$ in planes above and below this plane then cancel out, leaving only contributions from $m_+(r,t)$ in the plane at which $B_{d,+}(r,t)$ is calculated. Such in-plane magnetization contributions to $B_{d,+}(r,t)$ produce a field whose transverse components are parallel to $m_+(r,t)$.

To visualize the relative orientations of $m_+(r,t)$ and $B_{d,+}(r,t)$ for the spatial distribution of spin densities depicted in Figure 1, Figure 2a shows $m_+(r,t)$ and $B_{d,+}(r,t)$ at $t = 0$ for two voxels taken from the same xy -plane, one from region I and the other from region O. Unlike $B_{d,+}(r,t)$ in the one-dimensional model, $B_{d,+}(r,0)$ in Figure 2a deviates from the orientation of $m_+(r,0)$, which may be explained as follows. The different lengths of the magnetization vectors in regions I and O result in incomplete cancellation of $m_+(r,0)$ from different xy -planes along the z -axis when summed over the sample (eq 2), leading to a nonzero contribution to $B_{d,+}(r,0)$ in a given xy -plane from $m_+(r,0)$ in other transverse planes along the z -axis, which fan out in different directions due to modulation under the gradient. As a result, $B_{d,+}(r,0)$ is no longer aligned with $m_+(r,0)$ in a given xy -plane. This effect is especially pronounced near the interface between regions I and O, because the contributions to the DDF in these voxels come from a larger number of magnetization vectors whose individual contributions remain uncanceled.

Due to the difference in length between $m_+(r,0)$ in the two regions, the vector sum of $m_+(r,0)$ from planes above and below

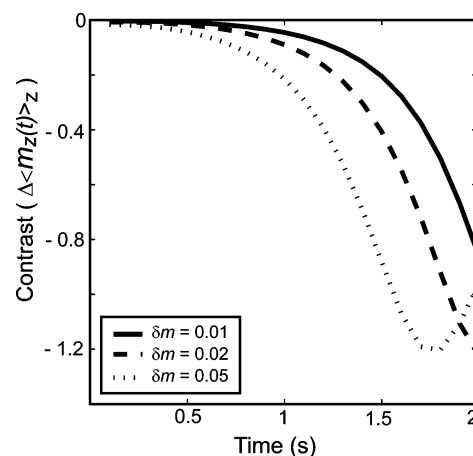


Figure 3. Contrast under the DDF only, as measured by $\Delta\langle m_z(t) \rangle_z \equiv \langle m_z(r_0,t) \rangle_z - \langle m_z(r_1,t) \rangle_z$, where $\langle m_z(r,t) \rangle_z$ represents the integral of m_z along the z -direction for a voxel at position r , with $(x_0, y_0) = (16, 16)$ and $(x_1, y_1) = (30, 30)$, for varying spin density differences δm . The pulse sequence and parameters are the same as in Figure 1.

$m_+(r,0)$ in a given xy -plane causes the phase angles between $B_{d,+}(r,0)$ and $m_+(r,0)$ to take on opposite signs in the respective regions (Figure 2a). The difference in phase angles between $m_+(r,0)$ and the corresponding $B_{d,+}(r,0)$ in the two regions causes $m_+(r,0)$ to tilt toward the $\pm z$ -axis, which in turn enhances the difference in m_z between the two regions while preserving $\langle m_z \rangle$ (averaged over the whole sample), which is a constant of the motion under $B_d(r,t)$. The increase in $\Delta\langle m_z \rangle_z$ leads to differences in $B_{d,z}(r,t)$ between the two regions. Due to the conservation of the z component of the total magnetization, $\langle m_z \rangle$, the overall change in $m_z(r,t)$ per voxel in region O is less than that in region I, which has a smaller contribution to the total magnetization. Therefore, $B_{d,z}(r,t)$ is greater in region I, and $m_+(r,t)$ in region I precesses more quickly, subtending a larger angle with respect to its initial orientation compared to $m_+(r,t)$ in region O, as captured in Figure 2b. As the directions of $m_+(r,t)$ in the two regions start to differ, the resulting magnetization configuration gives rise to increased phase angles between $m_+(r,t)$ and $B_{d,+}(r,t)$, the signs of which remain different for regions I and O (Figure 2b). As a result, $B_{d,+}(r,t)$ forces $m(r,t)$ even farther apart, thereby propagating the growth of $\Delta\langle m_z \rangle_z$ through a positive feedback cycle. Feedback-based contrast enhancement mediated by the DDF thus gives rise to exponentially fast growth of contrast due to small differences in spin density, as shown in Figure 3.

The DDF can also be used to enhance contrast due to small differences in precession frequency. When the model system consists of two regions differing by $\delta\omega$, the magnetization configuration formed by $[\theta_x - (GT)_z]$ is only modulated along the z -axis at $t = 0$. For $t > 0$, the difference in precession frequency between the two regions causes the phases of $m_+(r,t)$ in one region to shift with respect to the phases of $m_+(r,t)$ in the other, when compared for a given xy -plane. Although the $B_{d,+}(r,t)$ calculated by eq 2 in regions I and O point in slightly different directions, the $B_{d,+}(r,t)$ in both regions are oriented in a direction intermediate between those of $m_+(r,t)$ in region I and $m_+(r,t)$ in region O. As a result, the phase angles between $B_{d,+}(r,t)$ and $m_+(r,t)$ in the two regions have opposite signs, and $B_{d,+}(r,t)$ tilts $m(r,t)$ toward the $\pm z$ -directions in regions I and O. Following the dynamics described previously for differences in spin density, as $\Delta\langle m_z \rangle_z$ increases, $B_{d,z}(r,t)$ in the respective regions also differ, leading to an increase in the phase angles between $B_{d,+}(r,t)$ and $m_+(r,t)$ in both regions. $\Delta\langle m_z \rangle_z$ thus grows rapidly through positive

feedback mediated by $\delta\omega$ and the difference in m_z . For larger $\delta\omega$, the contribution of $m_+(r,t)$ in each region to $B_{d,+}(r,t)$ in the other is effectively averaged out if $1/\tau_d \ll \delta\omega$. The feedback process for differences in precession frequency under the DDF is thus most effective for small $\delta\omega < 10$ Hz.

Optimizing contrast enhancement under the DDF for small differences in spin density δm or precession frequency $\delta\omega$ requires carefully considering the stability properties of helical magnetization distributions prepared by $[\theta_x - (GT)_z]$. For example, when $\theta = 90^\circ$, the DDF does not effectively amplify contrast due to δm or $\delta\omega$, which may be understood by noting that a comparable magnetization helix prepared by $[(90^\circ)_x - (GT)_z]$ with uniform spin density is actually stable under the DDF.¹¹ Furthermore, the initial growth of contrast is identical for flip angles symmetric about $\theta = 90^\circ$, due to the symmetry in the resulting field orientations in the two regions. The growth in the contrast depends on the phase difference between $B_{d,+}$ and m_+ in the two regions immediately after $[\theta_x - (GT)_z]$. Numerical simulations show that contrast enhancement is more pronounced for flip angles close to $\theta = 100^\circ$ under the DDF for which the phase difference between the initial transverse components of the DDF and magnetization is largest.

IV. Radiation Damping

Radiation damping is a macroscopic feedback field that acts back on the solvent magnetization to oppose the induced free-induction decay (FID) current in the receiver coil, as dictated by Lenz's law.⁴ Radiation damping exerts a torque to nutate the net magnetization back to the $+z$ -axis along the surface of the Bloch sphere at a rate proportional to the average transverse magnetization $\langle m_+ \rangle$. The radiation damping field is given by¹³

$$\gamma B_{r,+}(t) = \frac{1}{\tau_r} \langle im_+(r,t) \rangle e^{-i\psi} \quad (4)$$

where the radiation damping time constant $\tau_r = 2/(\gamma\mu_0\eta M_0 Q)$,⁴ η is the sample filling factor, and Q is the probe quality factor. The phase ψ of $B_r(t)$ is assumed to lag behind that of $\langle m_+ \rangle$ by 90° , corresponding to $\psi = 0$; deviations from $\psi = 0$ decrease the effective torque applied to $m_+(r,t)$ by $B_r(t)$.¹⁴

The radiation damping field may be employed to enhance contrast due to spatial variations in precession frequency. Assume the magnetization in the two regions of the model system differ in precession frequency by $\delta\omega$. Following a θ_x hard pulse, where θ is close to 180° , the system evolves under radiation damping. The small net transverse magnetization present immediately after the pulse activates $B_r(t)$, which starts to rotate the net magnetization toward the $+z$ -axis. Due to the difference in precession frequency between the two regions, $m_+(r,t)$ in the two regions begin to precess out of phase, and $\langle m_+ \rangle$ lies between the $m_+(r,t)$ in regions I and O. As a result, $B_r(t)$, which depends on $\langle m_+ \rangle$, is no longer 90° phase-shifted from $m_+(r,t)$ in either region and excites $m_+(r,t)$ off-resonantly in both regions. However, $B_r(t)$ is closer to resonance with the magnetization in region O, which has a greater contribution to the total magnetization. Thus, $B_r(t)$ acts more selectively on $m_+(r,t)$ in region O, nutating the magnetization in this region toward $+z$ and initiating the growth of $\Delta\langle m_z \rangle_z$. As $B_r(t)$ excites $m(r,t)$ in region O more effectively, the proportional contribution of $m_+(r,t)$ in this region to $\langle m_+ \rangle$ increases, thereby reinforcing the selectivity of $B_r(t)$ for $m(r,t)$ in region O. At the same time, $m(r,t)$ in region I slips farther off resonance with respect to $B_r(t)$. The actual trajectories of $m(r,t)$ averaged over each region under radiation damping are shown in Figure 4. Through this

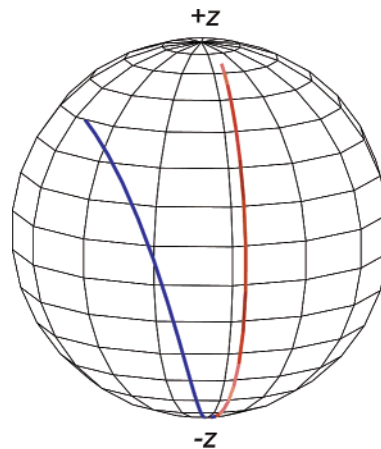


Figure 4. Three-dimensional trajectories of the bulk magnetization vectors for regions I (blue) and O (red) along the Bloch sphere under radiation damping following the pulse sequence shown in Figure 5. The magnetization vector for region I moves farther away from resonance with time.

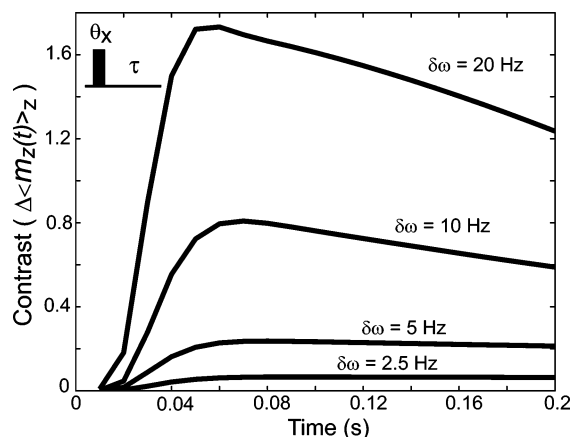


Figure 5. Contrast under radiation damping only, as measured by $\Delta\langle m_z(t) \rangle_z$, for varying precession frequency differences $\delta\omega$ following the pulse sequence shown ($\theta = 175^\circ$, $\tau_r = 8$ ms).

positive feedback process, Δm_z between the two regions grows as a power law in the initial time period ($t = 0$ – 0.05 s) (Figure 5).

Contrast enhancement under radiation damping was demonstrated experimentally on a cylindrical phantom with two spatial components varying in magnetic susceptibility: pure water in a 5-mm tube, and a 5% aqueous solution of acetone in an inner capillary. Figure 6 shows representative images and cross-sections of $\langle m_z \rangle_z$ at different evolution times τ under radiation damping. The imaged longitudinal magnetization appears relatively uniform immediately after the initial 175° hard pulse. As the magnetization in the two regions return to $+z$ under radiation damping, the water magnetization in the outer region is more effectively excited by $B_r(t)$ than the acetone/water magnetization in the inner region due to differences in magnetic susceptibility between the two solutions. The profiles of $\langle m_z \rangle_z$ plotted in Figure 6e illustrate the rapid growth of $\langle m_z \rangle_z$, characteristic of the dynamics under radiation damping.

The maximum contrast enhancement that the radiation damping field can provide depends on the initial flip angle θ of the applied pulse, the fractional volume occupied by the regions with different frequencies, and the frequency difference $\delta\omega$ between the regions of interest. For θ approaching 180° , the radiation damping field acts over a longer period of time to enhance contrast before the system reaches equilibrium. The

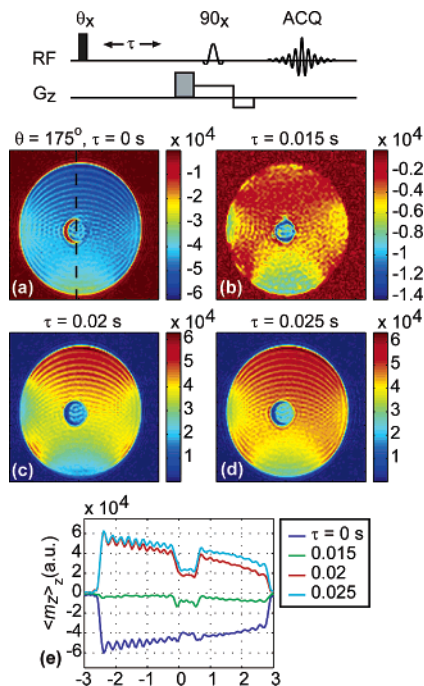


Figure 6. Experimental contrast enhancement under radiation damping following the pulse sequence shown at top. Images were taken of a cylindrical phantom consisting of water in a 5-mm tube with an inner capillary (0.5-mm outer diameter) of 5% acetone solution for flip angle $\theta = 175^\circ$ and evolution times τ of: (a) 0 s; (b) 0.015 s; (c) 0.02 s; and (d) 0.025 s. (e) Cross-sections of $\langle m_z \rangle_z$ for the images in (a)–(d), taken through the center of the sample, as indicated by the dotted line in (a). The strength of the first gradient was 5 G·ms/cm, whereas the second gradient was a crusher gradient designed to eliminate the net transverse magnetization. The selective 90° pulse was applied to image the longitudinal magnetization. Images were acquired using echo planar imaging with a field of view of 2 cm, slice thickness of 15 mm, and matrix size of 256×128 . The ridges seen in the images and profiles were attributed to Gibbs-ringing artifacts.

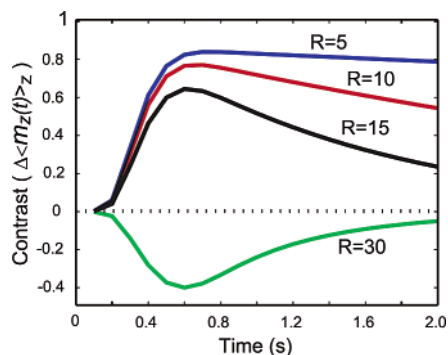


Figure 7. Contrast under radiation damping only, with an inner cylinder of varying radius (R) for the same pulse sequence as in Figure 5 ($\theta = 175^\circ$, $\tau_r = 8$ ms, $\delta\omega = 10$ Hz). The radius (R) is given in units of number of voxels, where the side of each voxel is 0.00734 mm.

radiation damping field acts more selectively on a region with greater fractional volume, and therefore, the difference in fractional volumes between two regions also determines the amount of contrast achieved. Figure 7 shows that a greater difference in fractional volume leads to greater contrast. The sign of the contrast changes when the magnetization in region I occupies a greater fractional volume (the curve corresponding to $R = 30$ in Figure 7). Notice from the Figure 7 that the contrast decreases at longer times when the inner cylinder has a larger radius, which can be explained as follows. The contrast reaches a maximum when the magnetization in region O is very close

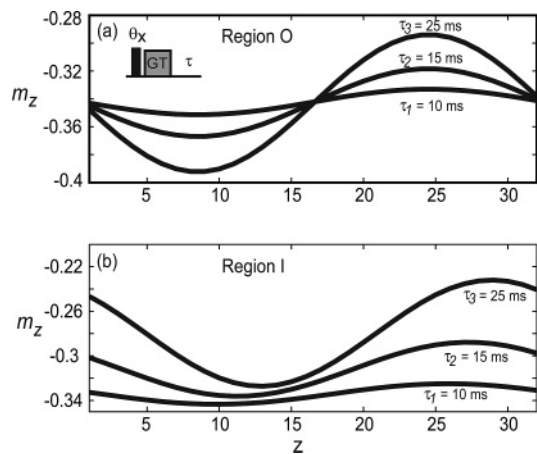


Figure 8. m_z for a line of lattice points along the z -axis, taken at different evolution times τ ($\tau_1 = 10$ ms, $\tau_2 = 15$ ms, $\tau_3 = 25$ ms), for evolution under the joint feedback fields of the DDF and radiation damping, following the pulse sequence shown ($\theta = 110^\circ$, $(GT)_z = 5$ G·ms/cm, $\tau_d = 69$ ms, $\tau_r = 8$ ms). (a) Line of lattice points in region O, taken away from the interface between regions I and O. (b) Line of lattice points in region I.

to the $+z$ axis. Beyond this time, the magnetizations in region I are excited more selectively, as these magnetizations now have larger m_+ and therefore contribute more to $\mathbf{B}_r(t)$. The selectivity of this excitation increases with an increase in the fractional volume of region I, which results in a proportional decrease in contrast as the magnetization in region I also approaches $+z$ at long times. The dependence of $\Delta\langle m_z(t) \rangle_z$ on the frequency difference is shown in Figure 5 for representative values of $\delta\omega$. For larger $\delta\omega$, $\mathbf{B}_r(t)$ becomes more selective for the magnetization in regions that have a greater contribution to the total magnetization, resulting in better contrast. However, the maximum contrast attainable under radiation damping is limited when the frequency difference $\delta\omega$ between two regions becomes very small, i.e., $\delta\omega < 10$ Hz. Such limitations may be overcome by exploiting contrast enhancement under the joint action of radiation damping and the DDF, which is discussed in the next section.

V. Joint Feedback Fields

Under the joint action of the DDF and radiation damping, the local field is described by a nonlinear Bloch equation that combines eqs 1, 2, and 4.¹⁵ The instability of certain magnetization configurations in the presence of the joint feedback fields can be used to amplify contrast due to slight differences in precession frequency. The dynamical process giving rise to better contrast under the joint feedback fields is more involved than the mechanisms leading to contrast enhancement under the individual feedback fields and is described as follows. As in the case of radiation damping, assume the model system has two compartments with a difference in precession frequency $\delta\omega$ between them. The preparation sequence $[\theta_x - (GT)_z]$ modulates the transverse magnetization into a helical configuration. Following the crusher gradient, a small net $\langle m_+ \rangle$ may survive, e.g., due to gradient imperfections, and activate the radiation damping field. $\mathbf{B}_r(t)$ rotates the modulated $m_+(r, t)$ toward $\pm z$ to varying extents, depending on the phase of $\langle m_+ \rangle$ relative to $m_+(r, t)$, to create a periodically modulated distribution of m_z along the z -axis. Figure 8a shows the variation in m_z for a set of lattice points along the z -axis in region O, far from the interface between the two regions. Although $\mathbf{B}_r(t)$ acts more effectively on $\mathbf{m}(r, t)$ in region O due to its greater weighted contribution to $\langle m_+ \rangle$, the effect of the DDF on $\mathbf{m}(r, t)$ in this

region away from the interface remains negligible at short times, such that the average of m_z along a line of voxels in the z -direction, $\langle m_z \rangle_z$, remains nearly constant in region O.

Near the interface between the two regions, the DDF effect becomes more significant. For the sample geometry modeled here, a larger fraction of the magnetization voxels in region I are closer to the interface than in region O. Thus, in the initial period, the dynamics in region I are dominated by the DDF. In this region, $B_{d+}(r, t)$ assumes a different direction in different planes but maintains the same magnitude throughout. The effect of the DDF is to tilt $\mathbf{m}(r, t)$ toward $+z$, in a manner analogous to the mechanism described for contrast enhancement due to precession frequency differences under the DDF alone (Section III). However, a small radiation damping field $\mathbf{B}_r(t)$ is also active. The resultant local field $\mathbf{B}(r, t)$ acting on the magnetization in different voxels along the z -axis depends on the relative orientation of $\mathbf{B}_r(t)$ and $\mathbf{B}_d(r, t)$ in each plane. When the feedback fields nearly cancel in a given xy -plane, the magnetization vectors in that plane tilt upward to a lesser extent, whereas when the two fields reinforce each other, the magnetization vectors flip upward to a greater extent (Figure 8b). Although m_z in different planes grows to varying extents, overall, $\langle m_z \rangle_z$ increases for the magnetization in region I. Because $\langle m_z \rangle_z$ in region O remains nearly constant during this time, the difference in $\langle m_z \rangle_z$ between the two regions continues to increase, giving rise to contrast enhancement, as measured by $\Delta\langle m_z \rangle_z$.

In region O, $\mathbf{B}_r(t)$ excites $\mathbf{m}(r, t)$ progressively to increase the amplitude of modulation in m_z along the z -axis, as seen in Figure 8a. The DDF generated by the modulation in m_z acts like a z -gradient, distorting the helical distribution of transverse magnetization to refocus more $\langle m_+ \rangle$, which further increases $|\mathbf{B}_r(t)|$. The interplay of $\mathbf{B}_r(t)$ and $\mathbf{B}_d(r, t)$ further distorts the magnetization helix and generates more $\langle m_+ \rangle$ in a positive feedback loop.¹⁶ Once $|\mathbf{B}_r(t)| \gg |\mathbf{B}_d(r, t)|$, the magnetization vectors in region O primarily nutate toward $+z$ under radiation damping. As contributions to $\langle m_+ \rangle$, and hence $\mathbf{B}_r(t)$, mainly derive from $\mathbf{m}(r, t)$ in region O, the joint reaction fields excite the magnetization in region O more effectively than the magnetization in region I. Consequently, beyond $\tau \approx 100$ ms, the magnetization vectors in region O rotate more quickly toward $+z$, leading $\Delta\langle m_z \rangle_z$ to change sign and continue increasing until $\langle m_+ \rangle$ reaches a maximum, corresponding to the steep rise in $\Delta\langle m_z \rangle_z$.

The increase in the clustering of $\mathbf{m}_+(r, t)$ in region O associated with maximal refocusing of $\langle m_+ \rangle$ is shown in Figure 9a,b. Because $\mathbf{B}_r(t)$ excites the magnetization in region I less effectively, the interplay of $\mathbf{B}_r(t)$ and $\mathbf{B}_d(r, t)$ on the magnetization in this region is not as significant; consequently, the distribution of $\mathbf{m}_+(r, t)$ vectors remain more uniformly modulated in region I compared to the magnetization in region O. Because the orientations of $\mathbf{m}_+(r, t)$ in region I are evenly distributed with respect to $\mathbf{B}_r(t)$, $\mathbf{B}_r(t)$ rotates the modulated $\mathbf{m}_+(r, t)$ symmetrically along the z -axis. This mechanism ensures that $\langle m_z \rangle_z$ remains small in region I, allowing the growth of $\langle m_z \rangle_z$ in region O due to the joint reaction fields to dictate the growth of $\Delta\langle m_z \rangle_z$ over time. At longer times, the DDF further modulates the magnetization in region O, such that $\langle m_z \rangle_z$ in this region begins to decrease, leading to a reduction in contrast.

Figure 10 shows the change in contrast with time for different frequency differences $\delta\omega$. Note that even for $\delta\omega$ as small as 2.5 Hz, significant contrast enhancement may be obtained under the joint feedback fields. Comparing the dependence of $\Delta\langle m_z \rangle_z$ in Figures 3 and 5 with the results in Figure 10 reveals the rich dynamics resulting from the interplay of $\mathbf{B}_d(r, t)$ and $\mathbf{B}_r(t)$. For

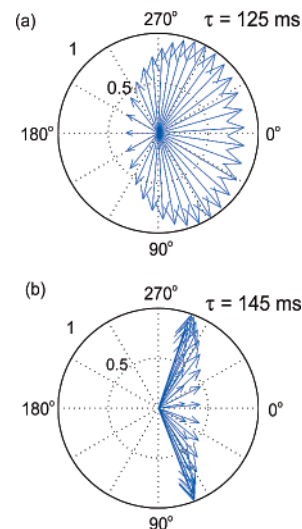


Figure 9. Transverse magnetization vectors $\mathbf{m}_+(r, t)$ in region O spanning one helix pitch along the z -axis, superimposed in each graph for (a) $\tau = 125$ ms and (b) $\tau = 145$ ms, for evolution under the joint action of radiation damping and the DDF following the pulse sequence shown in Figure 8.

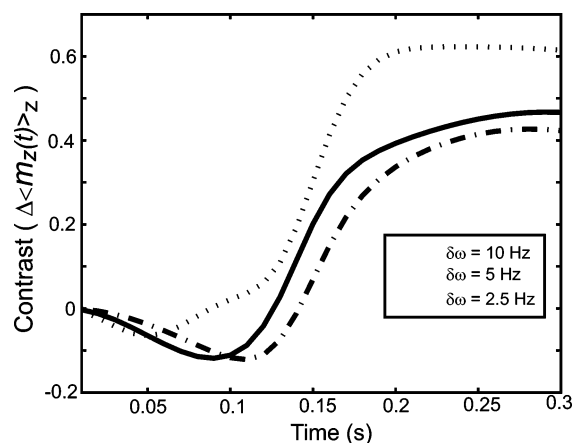


Figure 10. Contrast under the joint action of the DDF and radiation damping, as measured by $\Delta\langle m_z \rangle_z$, for varying precession frequency differences $\delta\omega$. The pulse sequence and parameters are the same as in Figure 8.

small frequency offsets ($\delta\omega < 5$ Hz), the DDF dominates at short times to generate negative contrast. As the magnetization helix unwinds to produce more $\langle m_+ \rangle$, $\mathbf{B}_r(t)$ becomes more significant and causes $\Delta\langle m_z \rangle_z$ to start increasing toward positive values. The negative contrast generated by $\mathbf{B}_d(r, t)$ is less pronounced for larger $\delta\omega$, as the transverse components of $\mathbf{B}_d(r, t)$ (responsible for the initial growth of $\Delta\langle m_z \rangle_z$) are effectively averaged out if $1/\delta\omega < \tau_d$. Instead, the effect of $\mathbf{B}_r(t)$ sets in much earlier to differentiate the two frequency components in collaboration with $\mathbf{B}_d(r, t)$.

Experimental demonstrations of contrast enhancement under the joint feedback fields of the DDF and radiation damping were carried out on a cylindrical phantom composed of two spatial regions: pure water in an outer 5-mm tube, and a 5% aqueous solution of ethanol in an inner capillary (Figure 11). Following the initial 120° pulse, the longitudinal magnetization across the sample is mostly uniform; deviations from uniformity can be attributed to slight differences in spin density between the two regions or nonuniform radio frequency (RF) excitation of the ethanol solution in the glass capillary. As the magnetization in both regions evolves under the joint reaction fields, the

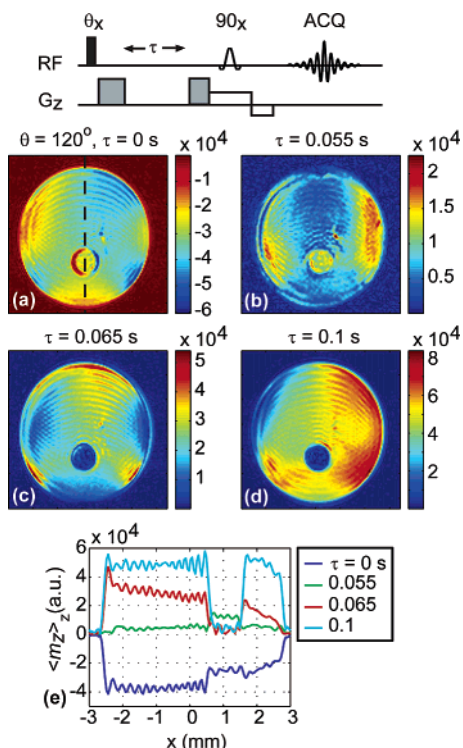


Figure 11. Experimental contrast enhancement under the joint action of the DDF and radiation damping following the pulse sequence shown at top. Images were taken of a cylindrical phantom consisting of water in a 5-mm tube with an inner capillary (1-mm outer diameter) of 5% ethanol solution for flip angle $\theta = 120^\circ$ and evolution times τ of: (a) 0 s; (b) 0.055 s; (c) 0.065 s; and (d) 0.1 s. (e) Cross-sections of $\langle m_z \rangle_z$ for the images in (a)–(d), taken through the center of the sample, as indicated by the dotted line in (a). The crusher gradient was designed to eliminate the net transverse magnetization following evolution under the joint reaction fields, whereas the selective 90° pulse was applied to image the longitudinal magnetization. Images were acquired using echo planar imaging with a field of view of 2 cm, slice thickness of 15 mm, and matrix size of 256×128 . The ridges seen in the images and profiles were attributed to Gibbs-ringing artifacts.

magnetization in the inner region first tilts upward due to the DDF. The gradual refocusing of more transverse magnetization under the joint feedback fields eventually causes radiation damping to predominate, resulting in the subsequent growth of $\langle m_z \rangle_z$ in the outer region toward $+z$.

VI. Discussion

We have shown that successively unstable magnetization configurations under the individual or joint feedback fields of radiation damping and the DDF are propagated through positive feedback. Coherent spatial variations in MR parameters that reflect the underlying morphology are amplified through the described nonlinear dynamical processes to enhance contrast. Smaller microscopic and macroscopic perturbations, including spin noise and experimental nonuniformities, may also be amplified on longer time scales, leading to signal irreproducibility^{15,16} as well as spatiotemporally chaotic spin motion¹⁷ in the presence of both reaction fields. The sensitivity of the amplification process to such small fluctuations may be tuned by judiciously designed pulse sequences that manipulate the magnetization into configurations of varying stability. For example, under radiation damping alone, the initiation of radiation damping by noise¹⁸ can be avoided by applying an initial $\theta = 175^\circ$ pulse, slightly away from the inverted state.

The effect of relaxation must be considered to compare the theoretical results discussed here with the outcome of experiments. Note that the longitudinal relaxation time, T_1 , is longer than the transverse relaxation time, T_2 , especially in biological samples.¹ The inclusion of the longitudinal relaxation term in eq 1 in the presence of radiation damping only does not appreciably change the magnitude of the resulting contrast, as the time scale within which the contrast grows in this case is much shorter (~ 100 ms) than T_1 (~ 1 – 2 s). The effect of transverse relaxation is also minimal on the radiation damping induced contrast because the transverse relaxation does not affect the longitudinal component of magnetization directly. T_2 relaxation indirectly shortens m_z as the magnetization nutates through the transverse plane. However, this indirect effect is small during the short time scale within which the contrast reaches maximum under the radiation damping field. The time scale of contrast enhancement under the DDF only as well as under the joint feedback fields is comparatively longer. Consequently, in these cases, spatial variations in T_1 may affect the net contrast as the growth of m_z is also affected by T_1 relaxation. In particular, a smaller T_1 relaxation time for magnetizations in region O leads to additional growth in the contrast due to the expedited return of m_z to $+z$ under both feedback fields and T_1 relaxation. Depending on the time scale of transverse relaxation, this additional enhancement may be counteracted partially or completely due to the indirect effect of T_2 relaxation on the longitudinal component of magnetization. Overall, relaxation has a minimal effect on the radiation damping induced contrast but may cause the contrast enhancement under the DDF only and the joint feedback fields to change depending on the time scale of T_1 and T_2 relaxation.

The time scales and physical constraints of relaxation must be considered when determining the feedback mechanism of choice for experiments. Because the DDF enhances contrast due to small differences in spin density or precession frequency over longer evolution periods ($\tau \approx 1.5$ – 2 s), this contrast enhancement mechanism may be more applicable to systems with long T_2 relaxation times. Under the radiation damping field, contrast enhancement due to resonance frequency differences develops on a time scale that is more accessible experimentally and has been shown to be particularly suited for biological samples with short T_2 relaxation times. However, the amplification of contrast through radiation damping may be less efficient for smaller $\delta\omega$. The joint feedback fields can enhance contrast in such cases, as has been demonstrated in experiments on phantoms and in vitro human brain tissue (unpublished results).

Understanding the complex dynamics leading to feedback-based contrast enhancement may guide the development of pulse/gradient combinations that mimic the amplification processes described here, thereby introducing external means of controlling the underlying spin dynamics. For example, as radiation damping is simply an RF field generated by the receiver coil through the sample magnetization, complex series of soft pulses with varying phases and frequencies may be designed to imitate and perhaps even improve upon the selectivity of the radiation damping field for different frequency components, particularly in cases in which radiation damping is weak or absent. In addition, contrast enhancement under the joint reaction fields may be reproduced by noting that the essential role of the DDF in generating contrast in the presence of radiation damping is to refocus the modulated magnetization. Similar refocusing can be achieved alternatively through magnetic field inhomogeneity or by applying a weak linear gradient along the z -axis. Because the strength of an applied

linear gradient can be adjusted at will, such a scheme would afford an alternative to contrast enhancement when the DDF is not present.

VII. Conclusion

We have proposed and elucidated the detailed mechanisms for amplifying contrast due to small spatial variations in MR parameters through the individual and joint feedback fields of the DDF and radiation damping. This understanding provides insight into the use of such feedback fields in current MRI and MR microscopy experiments and inspires the future design of pulse sequences that may ultimately grant the user control in tuning the contrast amplification factor, thereby surmounting specific experimental constraints.

Acknowledgment. This work was supported by the Camille and Henry Dreyfus Foundation (NF-01-078 and TC-05-053), Research Corporation (RI0781), NSF (CHE-0349362 and CHE-0116853), donors of the Petroleum Research Fund (ACS-PRF 41355-G6), and NSF Graduate Research Fellowship Program (S. Y. H.).

References and Notes

- (1) Haacke, E. M.; Brown, R. W.; Thompson, M. R.; Venkatesan, R. *Magnetic Resonance Imaging: Physical Principles and Sequence Design*; Wiley: New York, 1999.
- (2) Callaghan, P. T. *Principles of Nuclear Magnetic Resonance Microscopy*; Oxford University Press: Oxford, 1991.
- (3) Deville, G.; Bernier, M.; Delrieux, J. M. *Phys. Rev. B* **1979**, *19*, 5666.
- (4) Bloembergen, N.; Pound, R. V. *Phys. Rev.* **1954**, *95*, 8.
- (5) Abragam, A. *Principles of Nuclear Magnetism*; Oxford University Press: Oxford, 1961.
- (6) Enss, T.; Ahn, S.; Warren, W. S. *Chem. Phys. Lett.* **1999**, *305*, 101.
- (7) Lee, S.; Richter, W.; Vathyam, S.; Warren, W. S. *J. Chem. Phys.* **1996**, *105*, 874.
- (8) Marques, J. P.; Bowtell, R. *Concepts Magn. Reson.* **2005**, *25B*, 65.
- (9) Warren, W. S.; Lee, S.; Richter, W.; Vathyam, S. *Chem. Phys. Lett.* **1995**, *247*, 207.
- (10) Jeener, J. *Phys. Rev. Lett.* **1999**, *82*, 1772.
- (11) Jeener, J. *J. Chem. Phys.* **2002**, *116*, 8439.
- (12) Garrett-Roe, S.; Warren, W. S. *J. Magn. Reson.* **2000**, *146*, 1.
- (13) Vlassenbroek, A.; Jeener, J.; Broekaert, P. *J. Chem. Phys.* **1995**, *103*, 5886.
- (14) Huang, S. Y.; Anklin, C.; Walls, J. D.; Lin, Y.-Y. *J. Am. Chem. Soc.* **2004**, *126*, 15936.
- (15) Lin, Y.-Y.; Lisitza, N.; Ahn, S.; Warren, W. S. *Science* **2000**, *290*, 118.
- (16) Huang, S. Y.; Walls, J. D.; Wang, Y.; Warren, W. S.; Lin, Y.-Y. *J. Chem. Phys.* **2004**, *121*, 6105.
- (17) Datta, S.; Huang, S. Y.; Lin, Y.-Y. *J. Chem. Phys.* **2006**, *124*, 154501.
- (18) Augustine, M. P. *Prog. Nucl. Magn. Reson. Spectrosc.* **2002**, *40*, 111.